Journal of Materials Chemistry A

ROYAL SOCIETY OF CHEMISTRY

PAPER

View Article Online
View Journal | View Issue

Cite this: J. Mater. Chem. A, 2025, 13, 26610

Kinetics of CO_2 adsorption on UTSA-16(Zn) metal–organic framework: thermal, compositional, and geometrical effects†

Sanad Altarawneh ‡ and John Luke Woodliffe ‡*

Capturing CO_2 from point sources is a necessary step to limit the negative impacts of climate change. Metal–Organic Frameworks (MOFs), known for their exceptionally high surface areas and porosities, have demonstrated huge promise for environmental pollution control. The next stage of their application requires the design of equipment and materials capable of performing CO_2 adsorption optimally and efficiently at scale. However, this requires an in-depth understanding of the kinetics associated with CO_2 adsorption on MOFs under different circumstances (different geometries (pellets), compositions and temperatures). We present the first detailed kinetic study of the adsorption of CO_2 on MOF UTSA-16(Zn), a strong potential candidate for industrial-scale CO_2 capture, in the presence of different polymer binders and at different temperatures. Non-linear regression data fitting confirmed that a mixed order model was most able to describe the adsorption data, suggesting a combined controlling nature of surface adsorption and diffusion. Adsorption rate constants had an Arrhenius temperature dependency, and the calculated temperature independent kinetic parameters (activation energy and pre-exponential factor) allow the calculation of adsorption rates at any required design temperature. A potential reactor design and case study are also presented. The results provide valuable input to inform future design of adsorbent systems for CO_2 capture, facilitating the transition of MOFs to industrial scale applications to address urgent environmental challenges.

Received 28th April 2025
Accepted 14th July 2025

DOI: 10.1039/d5ta03364k

rsc.li/materials-a

1. Introduction

Climate change is expected to have a significant negative impact on the environment and our society.[1] CO_2 capture has been identified as a necessary technology to achieve net-zero emissions limiting the impacts of climate change by capturing CO_2 at the source and preventing it from entering the atmosphere.[2] The current available technology for this process is known as amine scrubbing, however, large energy requirements for regenerating the amine absorbents have severely limited industrial adoption.[3] An alternative class of materials known as Metal–Organic Frameworks (MOFs) have emerged as a promising solution, offering significantly reduced energy demands for regeneration. This reduction in energy is due to CO_2 being physically adsorbed to the surface of the materials, rather than bound by chemical bonds as with the amine solvents.[4] MOFs contain nodes of metal ions or clusters held together by organic molecules as linkers between the nodes.[5] Since the metal ions and organic molecules can be varied, the resulting MOFs demonstrate tuneable properties with high internal surface areas, which can be tailored to a range of applications from gas storage to biomedicine.[6–10] MOFs have demonstrated highly beneficial properties for use in CO_2 capture applications, including high CO_2 capacities and high selectivity for CO_2 over other gases such as N_2.[11] One MOF with strong potential for industrial-scale CO_2 capture is UTSA-16(Zn) (UTSA = University of Texas at San Antonio), composed of Zn clusters and citrate linkers ($C_{12}H_8KO_{14}Zn_3$).[12] In addition to a high CO_2 capacity and selectivity, UTSA-16(Zn) has shown high stability to moisture and acid gases, low reagent costs and scalable microwave and continuous-flow synthesis routes.[13–15] UTSA-16(Zn) has also found application as a fluorescence detector for SO_2,[16] and its CO_2 capture properties can be further tuned through cation replacement.[17]

Despite the development of scalable synthesis and activation routes for UTSA-16(Zn) and other MOF/MOF composites, they are typically still produced as dry powder formulations.[18–21] However, for CO_2 capture and other large-scale applications, the powders need to be formed into granules and/or pellets to prevent large pressure drops across packed bed reactors and to improve general handling.[22] Pressure compaction has been typically used to form pellets for other materials, however, with MOFs, the pressures can cause the highly porous structures to collapse, resulting in a loss of porosity and gas storage

Advanced Materials Research Group, Faculty of Engineering, University of Nottingham, Nottingham, NG7 2RD, UK. E-mail: luke.woodliffe1@nottingham.ac.uk

† Electronic supplementary information (ESI) available. See DOI: https://doi.org/10.1039/d5ta03364k

‡ These authors contributed equally to this work.

capacity.[23] Therefore, binders have been investigated as a solution to hold MOF powders together and provide mechanical stability to the pellets without the need for compaction. In particular, polymer based binders have been effective for producing MOF pellets since they can be easily processed using solvents (without the need for high temperature calcination), have low weights (minimising losses in gravimetric CO_2 capacity), are permeable to gases and can form hydrogen bonds to MOFs through polar chemical groups.[24,25] Although many studies have explored the impacts of shaping and binders on MOF properties,[23,25,26] and others have explored the adsorption kinetics of specific MOFs,[27–30] there have been very few in-depth studies on the impact of pelletisation with different binders on the kinetics of CO_2 adsorption. The first studies in this area have been produced in the last two years, considering kinetic effects for MOFs Al–BTC (btc = 1,3,5-benzenetricarboxylate), aluminium fumarate (AlFum) and ZIF-8 (ZIF = zeolitic imidazolate framework).[31,32] The ZIF-8 study used a binder mixture of 50 : 50 methylcellulose and bentonite at 20–30 wt%, which was found to significantly improve mechanical strength but caused a loss of surface area and slower CO_2 adsorption kinetics due to framework collapse.[31] The Al–BTC and AlFum study used sodium alginate, Septon and silica-sol binders, finding that the different binders had varying impacts on CO_2 kinetics.[32] The impacts on CO_2 kinetics from other binders and with different MOFs is still unknown. This underexplored area represents a significant knowledge gap since the kinetics of adsorption will have a large impact on the cycle time for packed bed adsorbers, influencing decisions such as reactor design and operational conditions. Herein, we present a unique study of the kinetics of CO_2 adsorption on UTSA-16(Zn) powder and pellets with polyvinyl alcohol (PVA), polyvinyl butyral (PVB) and polyvinylpyrrolidone (PVP) polymer binders. Each of these binders have been used to effectively formulate pellets with different MOFs, but in-depth kinetic analysis is missing for these binders and for UTSA-16(Zn).[24,33–38] This study includes isothermal adsorption scans at different temperatures to assess the impact of pelletisation and the various binders on rate constants, activation energies and pre-exponential factors associated with the adsorption phenomenon using a Mixed Order (MO) model rate equation. These results provide researchers and engineers in this field with valuable resource to inform future rational design of UTSA-16(Zn) and other adsorbent formulations for CO_2 capture, and enable the improved modelling of packed bed adsorbers to facilitate the transition of MOFs to industrial scale applications.

2. Adsorption kinetics

2.1. The rate equation

The degree of CO_2 adsorption is usually defined by the normalised molar quantity "q_t" which is the molar amount of adsorbed CO_2 per unit mass of MOF ($mmol_{-(CO_2)}\ g_{-(MOF)}^{-1}$); this will be reported as mmol g^{-1} subsequently. The rate of adsorption $\frac{dq_t}{dt}$ is related to the Arrhenius rate constant k and the adsorption model $f(q)$ as follows:

$$\frac{dq_t}{dt} = k \times f(q) \quad (1)$$

2.1.1. Pseudo first order (PFO). The most known and used adsorption model is the pseudo-first-order (PFO) first reported by Lagergren,[39] where the rate of adsorption is linearly related to the difference in adsorbed CO_2:

$$\frac{dq_t}{dt} = k_f \times (q_e - q_t) \quad (2)$$

where k_f is the PFO rate constant and q_e is the equilibrium adsorbed amount of CO_2 per unit mass of MOF. The differential form above is a separable ordinary differential equation (ODE) and can be presented in its integral form using the initial condition of $q_o = 0$ and $t = 0$:

$$q_t = q_e(1 - \exp(-k_f \times t)) \quad (3)$$

Usually, the rate constant is extracted by linear regression using the re-arranged form of eqn (3):

$$\ln(q_e - q_t) = \ln(q_e) - k_f \times t \quad (4)$$

A plot of $\ln(q_e - q_t)$ against t should yield a straight line with a slope of the PFO rate constant k_f.

2.1.2. Pseudo second order (PSO). In the pseudo-second-order (PSO) model, the rate is quadratically related to the difference in adsorbed amount. This model was initially introduced by Ho *et al.*[40] The rate equation is written as follows:

$$\frac{dq_t}{dt} = k_s \times (q_e - q_t)^2 \quad (5)$$

where k_s is the PSO rate constant. With a similar treatment to eqn (2) and (5) can be solved for the integral form of the adsorption capacity:

$$q_t = \frac{k_s q_e^2 t}{1 + k_s q_e t} \quad (6)$$

To extract the kinetic rate constant, eqn (6) can be linearised to the following:[41]

$$\frac{t}{q_t} = \frac{1}{k_s q_e^2} + \frac{t}{q_e} \quad (7)$$

Such that a plot of $\frac{t}{q_t}$ against t yields a straight line with a slope of $\frac{1}{q_e}$ and an intercept of $\frac{1}{k_s q_e^2}$ from which the PSO rate constant can be extracted. However, the accuracy of the linear regression approach was shown to be lacking.[42,43] Thus, non-linear regression for a more complicated model was used.

2.1.3. Mixed order (MO). Depending on the adsorption system, the controlling mechanism in certain situations is more complicated and can, in some cases, be convoluted. In that case, the PSO and PFO models alone fail to fit the data to high accuracy, though may fit the data partially (*i.e.*, during adsorption initiation or during the plateauing region towards

equilibrium). Hence, in this work, a Mixed Order (MO) model (described in ref. 44 and 45) will be used. In this model, both the first and second order models contribute to the adsorption rate, weighted by the value of their respective rate constants as follows:[41]

$$\frac{dq_t}{dt} = k_f \times (q_e - q_t) + k_s \times (q_e - q_t)^2 \quad (8)$$

Eqn (8) is the general kinetic rate equation which is more capable of describing more complex adsorption systems. However, to solve for the integral form, a more complicated treatment is required. Eqn (8) is considered a Bernoulli ODE.

After solving eqn (8), the final solution for the adsorption capacity function can be given as follows:

$$q_t = q_e \left(1 - \frac{1}{\frac{k_s}{k_f} q_e \left(\exp(k_f t) - 1\right) + \exp(k_f t)} \right) \quad (9)$$

Obtaining the values of k_f and k_s by linear regression is not possible due to the complicated nature of eqn (9). Hence, data fitting against experimental q_t values was performed using a non-linear regression approach by iteratively modifying the values of k_f and k_s for the best fit. From there, values of k_f and k_s were extracted at different temperatures.

2.2. The rate constant and the Arrhenius function

In addition to k_f and k_s, it is useful to report the rate of adsorption in terms of temperature independent kinetic parameters: the activation energy (E) and the pre-exponential factor (A). The Arrhenius rate constant can be written as follows:[46]

$$k(T) = A \times \exp\left(\frac{-E}{RT}\right) \quad (10)$$

Such that R is the universal gas constant (8.314 J mol^{-1} K^{-1}) and T is the temperature in kelvin. Hence, the rate constant in this work was extracted at different adsorption temperatures of 25, 40, 60 and 80 °C. The values of E and A were then extracted from the linearisation of eqn (10):

$$\ln k(T) = \ln(A) - \frac{E}{RT} \quad (11)$$

Using the equation above, one can extract E and A from the slope and intercept of the Arrhenius plot of $\ln k(T)$ against $\frac{1}{T}$.

The final kinetic equation in its differential and integral form can be obtained by substituting eqn (10) in eqn (8) and (9):

$$\frac{dq_t}{dt} = A_f \times \exp\left(\frac{-E_f}{RT}\right) \times (q_e - q_t) + A_s \times \exp\left(\frac{-E_s}{RT}\right) \times (q_e - q_t)^2 \quad (12)$$

$$q_t = q_e \left(1 - \frac{1}{\frac{A_s \times \exp\left(\frac{-E_s}{RT}\right)}{A_f \times \exp\left(\frac{-E_f}{RT}\right)} q_e \left(\exp\left(A_f \times \exp\left(\frac{-E_f}{RT}\right) t \right) - 1 \right) + \exp\left(A_f \times \exp\left(\frac{-E_f}{RT}\right) t \right)} \right) \quad (13)$$

Such that E_f, E_s, A_f, and A_s are the activation energy and the pre-exponential factor for the PFO and PSO rate constants, respectively. Eqn (13) is the final equation which shows how the adsorption capacity of the MOF (q_t) is related to temperature and time through a series of temperature independent parameters: E_f, E_s, A_f, and A_s.

3. Method

3.1. Materials

Reagents were all used as purchased and only deionised water was used. Polyvinyl pyrrolidone (M_w: 55 000), polyvinyl butyral, polyvinyl alcohol (M_w: 9000–10 000; 80% hydrolysed), potassium hydroxide (86.7%), citric acid monohydrate (≥99.0%), zinc acetate dihydrate (≥99.0%) were purchased from Merck. Ethanol (absolute, SpS grade) was obtained from Scientific Laboratory Supplies LTD, while methanol (≥99.9%) was obtained from Fisher Scientific.

3.2. Synthesis of MOF UTSA-16(Zn)

The MOF UTSA-16(Zn) was produced in powder form using a continuous flow reactor, custom-built using Vapourtec pumps (R2+/R4, SF-10), Idex fittings and PTFE tubing (OD: 3.2 mm, ID: 1.6 mm). Firstly, two solutions were prepared. One was a solution of $Zn(OAc)_2 \cdot 2H_2O$ (0.4 M), citric acid monohydrate (0.44 M) and KOH (1.32 M) in H_2O, and the other was pure ethanol. These solutions were pumped at 5 mL min^{-1} each into an arrowhead mixing tee (ID: 0.79 mm), and the resultant stream

heated to 120 °C for 5 minutes residence time through an oil bath heater coil (25 m). The suspension was cooled using a water bath (room temperature) and passed through a back pressure regulator (6 bar). The MOF product suspension was then collected, centrifuged, washed (4× MeOH) and dried (75 °C, overnight). The final UTSA-16(Zn) product was collected in the powder form (12.6 g, 71% yield).

3.3. Pelletisation of MOF UTSA-16(Zn)

UTSA-16(Zn) was formulated with different polymer binders and pelletised by extrusion. Pure binder solutions were prepared at 8 wt% by dissolving PVB in 8 : 2 EtOH : H_2O (10 mL) and PVA or PVP in 7 : 3 EtOH : H_2O (10 mL). Slurries of UTSA-16(Zn) in the polymer binder solutions (8 wt% PVA, PVP and PVB) were then prepared at 1 g mL^{-1} and extruded using a 5 mL syringe onto Petri dishes. The extrudates were then divided using a knife, dried at 100 °C for 10 minutes after which they were activated in a vacuum oven (120 °C, overnight). Adsorption analysis was performed for the UTSA-16(Zn) MOF powder and pelletised MOF with 8 wt% binders (please refer to the nomenclature in Table 1).

3.4. Chemical characterisation

3.4.1. X-ray diffraction (XRD). X-ray diffraction (XRD) patterns were measured at room temperature with a Bruker D8 Advance DaVinci from 5° to 45° 2θ, with a step size of 0.02° and a step time of 0.7 s. Bragg–Brentano geometry was used with a Lynxeye 1D detector and a Cu Kα radiation source ($\lambda = 0.15406$ nm) at 40 kV and 40 mA. Bruker DIFFRAC.EVA software was used for data interpretation with ICDD crystallographic database.

3.4.2. Fourier transform infrared spectroscopy (FT-IR). Infra-red spectra were taken on a Bruker Alpha II instrument equipped with a Platinum-ATR. The instrument contains a RockSolid™ interferometer, CenterGlow™ source and diode laser. Data were acquired over 24 scans in the range of 500–4000 cm^{-1} with a 4 cm^{-1} resolution and background subtraction.

3.4.3. Scanning electron microscopy (SEM). Scanning electron micrographs were recorded on a JEOL 7000F FEG-SEM at a working distance of 10 mm. Samples were coated with 10 nm of Ir prior to analysis and images were recorded in secondary electron mode with an acceleration voltage of 10–15 kV.

3.4.4. Transmission electron microscopy (TEM). Transmission electron micrographs were taken using a JEOL 2100Plus with a Gatan OneView camera and JEOL STEM detectors at 200 kV. A dry tumbling technique was used to deposit the samples onto holey carbon film for analysis.

3.4.5. Thermogravimetric analysis (TGA). CO_2 adsorption was measured through a gravimetric analysis method at atmospheric pressure on a TA Instruments TGA550 Discovery.[47] Powder and pellet samples were activated by heating to 120 °C under a flow of N_2 at 100 mL min^{-1}, held for 20 minutes then cooled to the relevant adsorption temperature. Once the adsorption temperature was reached, the gas was switched to CO_2 at a flow rate of 500 mL min^{-1}, and held for 10 minutes. The reasoning behind using a high flow rate of for CO_2 at 500 mL min^{-1} was to expose the material to 100% CO_2 concentration to omit the concentration effect on kinetics. The sample was then activated again under N_2 prior to the next adsorption cycle. CO_2 adsorption isotherms were performed for each sample at temperatures of 25, 40, 60, 80 °C.

Table 1 Nomenclature and images of materials used in this work

Name	Composition	Image
NB-MOF	No binder powder MOF	
PVA-P-MOF	Pelletised MOF + PVA (8 wt%)	
PVB-P-MOF	Pelletised MOF + PVB (8 wt%)	
PVP-P-MOF	Pelletised MOF + PVP (8 wt%)	

4. Results and discussion

4.1. Chemical analysis and MOF characterisation

The MOF UTSA-16(Zn) was synthesised *via* a continuous flow method as described earlier in Section 3.2, which is reported in detail elsewhere.[48] Fig. 1A shows the powder XRD pattern for the as-synthesised MOF, demonstrating high crystallinity in close alignment with the calculated pattern produced from the Crystallographic Information File with Mercury software.[49] The pattern shows characteristic peaks at 2$\theta \approx$ 7°, 11°, 14° and 16°, matching previous reports.[12,14] The MOF crystal structure is also shown to be unaffected by the extrusion pelletisation process (Fig. 1A). FTIR analysis in Fig. 1B supports the expected chemical composition of UTSA-16(Zn) with characteristic symmetric and asymmetric stretching vibrations of carboxylic groups around 1400 and 1580 cm^{-1}, respectively.[50] A broad hydrogen bonding peak is also observed around 3400 cm^{-1} which is assigned to hydroxyl groups. These results match the spectra of UTSA-16(Zn) from previous reports.[51] After pelletisation, the chemical structure of the MOF is shown to be unchanged,

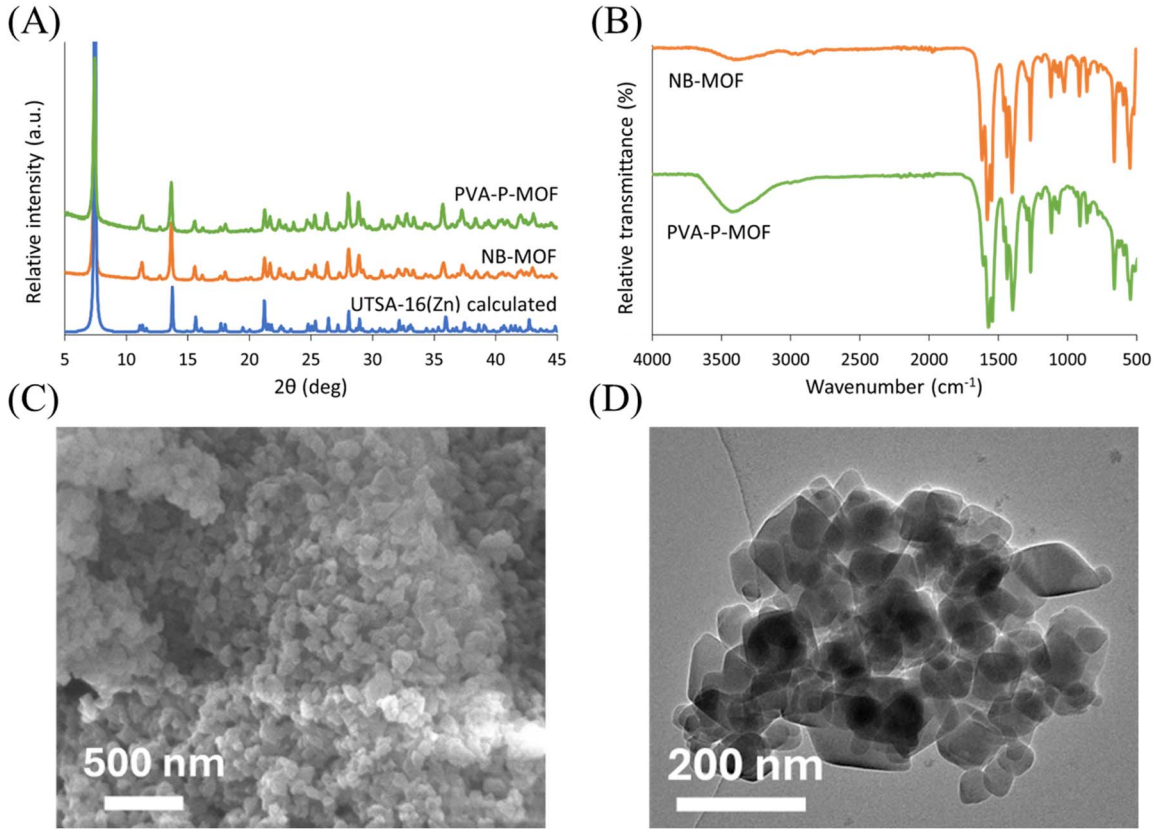

Fig. 1 (A) Experimental and calculated powder XRD patterns for UTSA-16(Zn) before pelletisation (NB-MOF) and after pelletisation with PVA binder (PVA-P-MOF) (B) ATR-FTIR spectra of UTSA-16(Zn) before pelletisation (NB-MOF) and after pelletisation with PVA binder (PVA-P-MOF) (C) SEM micrograph of Ir coated UTSA-16(Zn) particles, and (D) TEM micrograph of UTSA-16(Zn) particles on a holey carbon film.

though the broad hydroxyl peak increased in amplitude due to the hydroxyl groups in the PVA binder (Fig. 1B). SEM and TEM micrographs (Fig. 1C and D) show the MOF particle morphologies, revealing reasonable uniformity of approximately octahedral polyhedra around 50–100 nm. These morphologies are similar to what have previously been observed with different batch synthesis methods.[13,15]

4.2. Thermal behaviour and CO_2 adsorption isotherms

The CO_2 adsorption cycles for powdered MOF (NB-MOF) and MOF pelletised with different binders (PVA, PVB, and PVP) at temperatures of 25, 40, 60 and 80 °C are shown in Fig. 2. Several adsorption–desorption cycles are shown at different temperatures. Clearly, the equilibrium adsorbed amount of CO_2 (q_e) drops systematically going from 25 °C to 80 °C for all materials; higher temperatures result in lower adsorption capacities. More importantly, however, changing the geometry of the MOF from powder (NB-MOF) to pellets (PVA-P-MOF, PVB-P-MOF, PVP-P-MOF) results in a drop in q_e.

To better understand this trend, three replicates for the adsorption isotherms were performed for all the materials, and results of their equilibrium adsorption capacities are summarised in Fig. 3. All pelletised samples showed a drop in the CO_2 adsorption capacity of the MOF component compared to the pristine powdered MOF due to several factors. First, binders can cause a pore-blocking effect where they restrict the access of CO_2 to active pore sites in the MOF, resulting in a drop in adsorption capacity.[24,36,38] In addition, a decrease in capacity may be observed due to the mechanical pressure exerted on the MOF during extrusion pelletisation.[23] Finally, the formulation of the material in pellet form results in an overall drop in surface area which adds an additional thickness through which CO_2 has to travel before reaching the active site.

A noticeable variation in equilibrium adsorption capacity can be seen going from one binder type to another. Both PVB-P-MOF and PVP-P-MOF display higher adsorption capacities than that obtained for PVA-P-MOF at all temperatures. This is likely due to the additional pore-blocking nature of PVA compared to PVB and PVP, which has also been observed previously.[52]

The drop in CO_2 capacity of the pellets compared to the powdered MOF starts to diminish at higher temperatures (especially for PVB-P-MOF). This may be assigned to enhanced gas diffusivity at high temperature and/or thermal expansion of the material making more accessible pathways for the gas to reach active sites.

The trend appearing in Fig. 3 suggests that pelletising, while being crucial for development of practical adsorption systems (better material flowability, reduced pressure drop through beds, *etc.*), can hinder the adsorption capacity of the MOF which can clearly be seen in the case of PVA-P-MOF as an example.

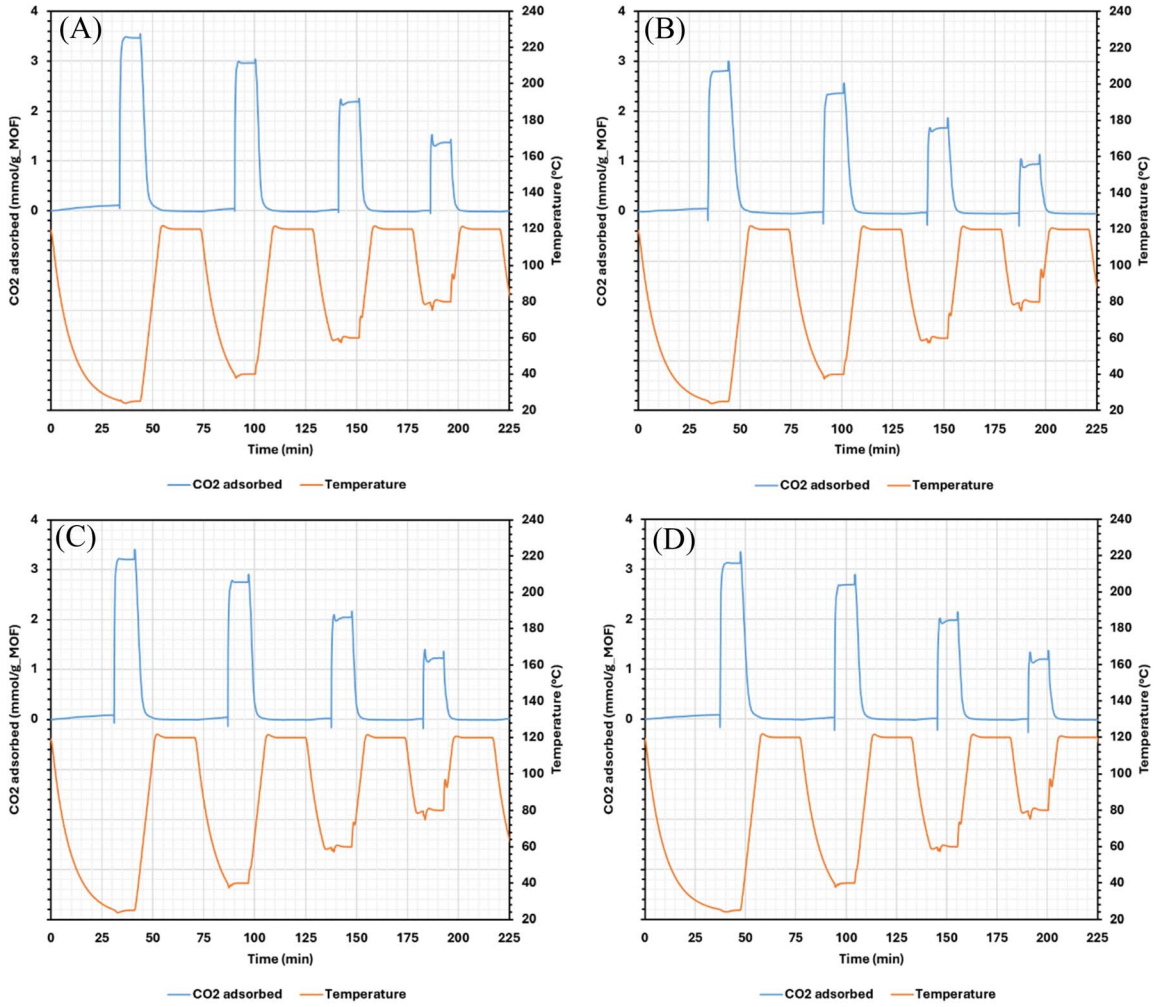

Fig. 2 CO_2 adsorption isotherms for (A) NB-MOF, (B) PVA-P-MOF, (C) PVB-P-MOF, and (D) PVP-P-MOF at temperatures of 25, 40, 60 and 80 °C.

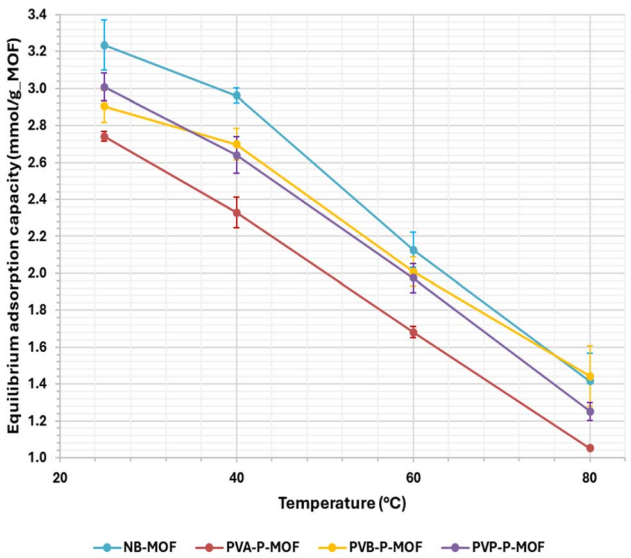

Fig. 3 Equilibrium CO_2 adsorption capacity of NB-MOF, PVA-P-MOF, PVB-P-MOF, and PVP-P-MOF at different temperatures.

4.3. Kinetics of CO_2 adsorption

4.3.1. The Arrhenius plots and kinetic parameters. Fitting the experimentally obtained rate constants with temperature allows the extraction of the temperature independent kinetic parameters (activation energy E and pre-exponential factor A). These parameters can then be used to predict adsorption rates at any required temperature (which can also be extrapolated for temperatures not reported here; <25 °C and >80 °C). In Fig. 4 and 5, a clear linear trend of the natural log of the rate constant with the reciprocal of temperature can be seen. This suggests that the rate constant associated with CO_2 adsorption on MOFs follows the Arrhenius function reported in eqn (10). The data fitting of the PFO and PSO rate constants (k_f and k_s) for NB-MOF, PVA-P-MOF, PVB-P-MOF, and PVP-P-MOF are presented in Fig. 4 and 5, respectively.

The Arrhenius plots appearing in Fig. 4 and 5 were used to extract the kinetic data reported in Table 2. The data in Table 2 can be used to predict adsorption rates and adsorption progress (q_t) when used in conjunction with eqn (12) and (13), respectively. The trend of the activation energy and pre-exponential factor with composition and geometry of the tested materials

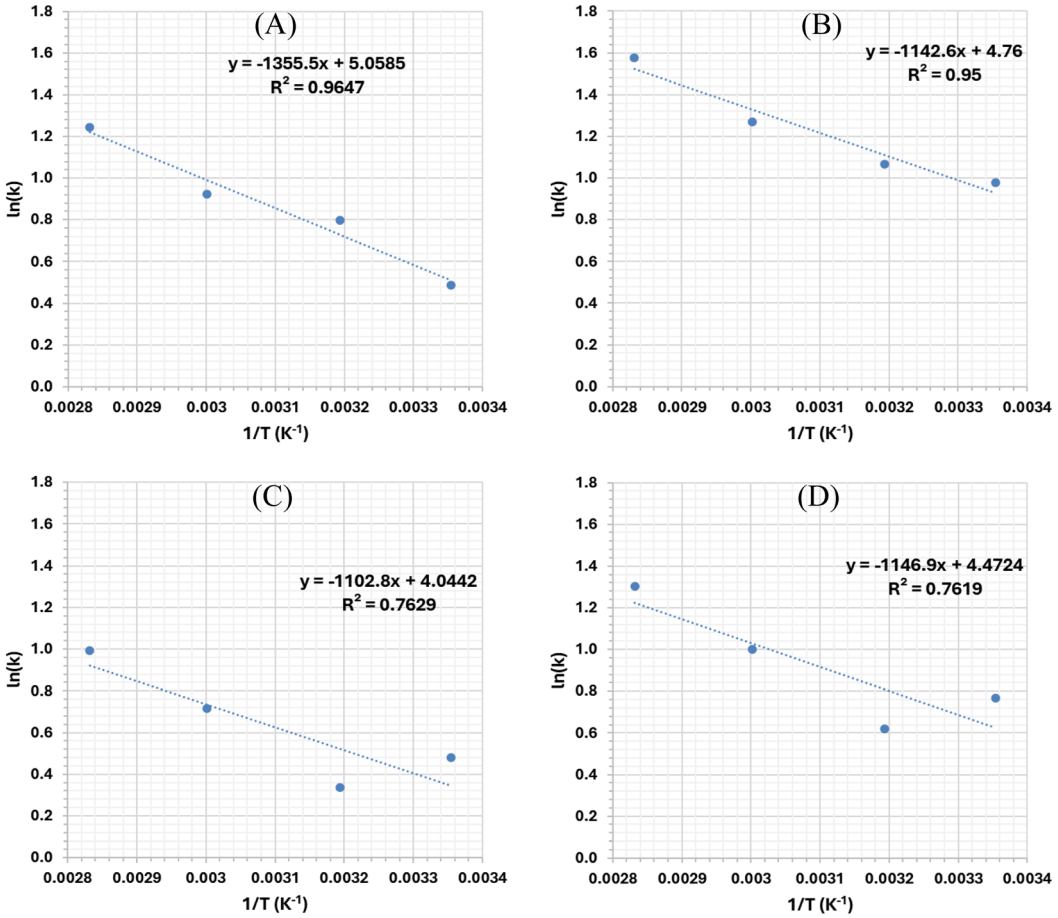

Fig. 4 Arrhenius plots of PFO rate constants for (A) NB-MOF, (B) PVA-P-MOF, (C) PVB-P-MOF, and (D) PVP-P-MOF against the reciprocal of temperature (units of k_f is min^{-1}).

is summarised in Fig. 6A and B. All the systems exhibited a mixed model (MO) adsorption nature whereby the adsorption rate depends on both PFO and PSO models, except for PVA-P-MOF which only showed a PFO rate dependence (*i.e.*, $k_s = 0$).

Despite the convoluted behaviour of adsorption (*i.e.*, being governed by PFO and PSO), the significance of the dominant model varies with adsorption progression; this is because the contribution of both k_f and k_s to the overall adsorption rate (eqn (8)) is weighed by the factors $(q_e - q_t)$ and $(q_e - q_t)^2$, respectively. These factors amount to significantly different values depending on the adsorption progress (see Fig. 7A). The $(q_e - q_t)^2$ factors exhibit much higher values initially, which then dip below the $(q_e - q_t)$ factors when the adsorption progresses further. This effect is reflected on the adsorption behaviour as presented in Fig. 7B.

At the initial stage of adsorption (<0.5 min), the PSO model fits the data well. However, going towards equilibrium (>1.5 min), the PFO model fits the experimental data more accurately. Such a result is in line with the trends in Fig. 7A showing a dominance of the PSO weighing factor $(q_e - q_t)^2$ below 0.3 min before PFO starts dominating towards equilibrium. Generally, PFO rate is known to describe diffusion, while PSO rate resembles the adsorption step on active sites.[45] Following this, and since at the initial stage more active sites are available, the PSO model would naturally dominate (Fig. 7B). As the adsorption progresses, the active sites become encapsulated within the body of the MOF, which can be considered similar to that described in the Shrinking Core Model (SCM) reported in Levenspiel 1998.[53] While the SCM was originally devised for reactive systems (chemical) and not adsorption (physical), the concept still holds since a passive outer layer is formed whether it is a chemical or a physical process. This leads to the PFO model being more representative towards equilibrium adsorption. This behaviour justifies the usage of the MO model where the effect of both PFO and PSO models are convoluted to track the adsorption progress in a more accurate manner.

As previously discussed, PVA-P-MOF is the only system which was entirely described by a PFO model. PVA binder is thus believed to have completely encapsulated the MOF creating a barrier through which the CO_2 needs to diffuse. Hence the process was diffusion controlled showing dependence only on the PFO model. This result is in agreement with the equilibrium adsorption capacities reported in Fig. 3, in which PVA-P-MOF showed the lowest adsorption capacity, potentially due to blockage of active sites by the binder resulting in an overall hindrance in adsorption.

The reliability of the extracted kinetic data reported in Table 2 was tested by overlaying it against experimentally obtained

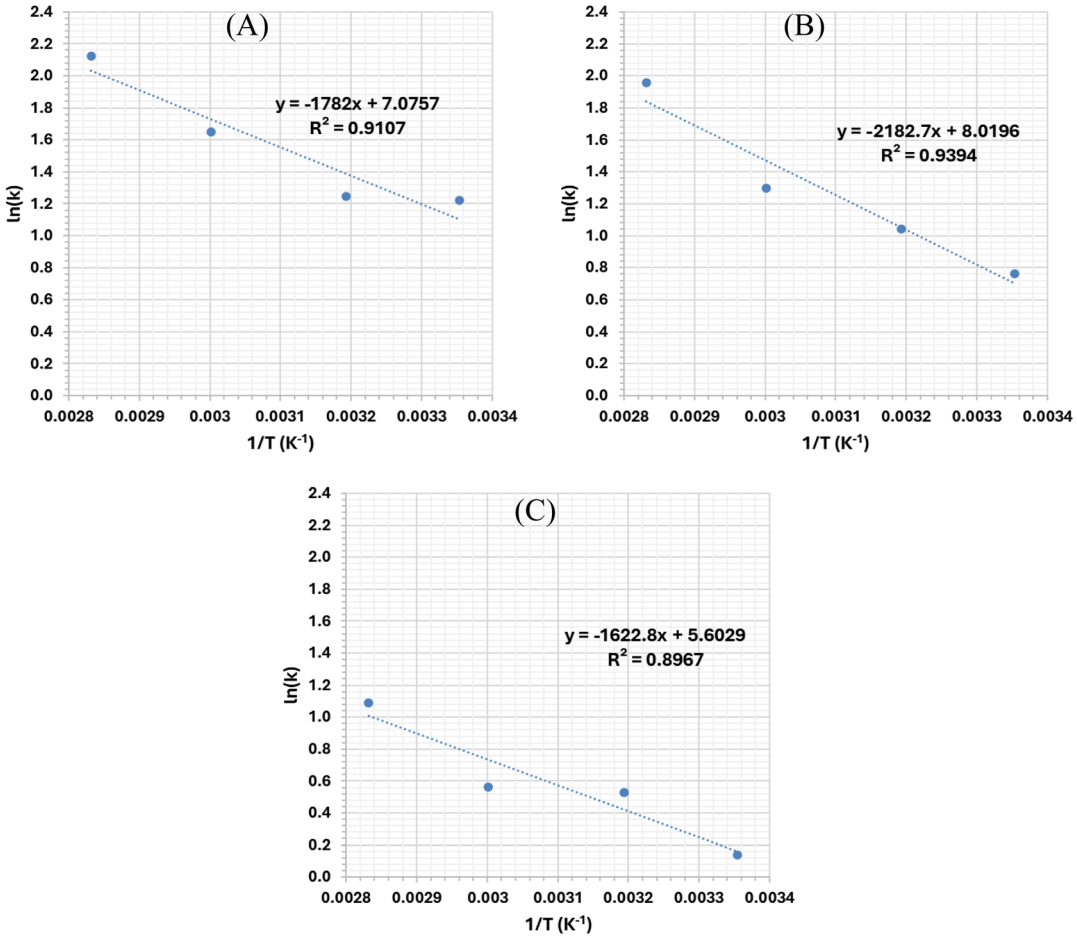

Fig. 5 Arrhenius plots of PSO rate constants for (A) NB-MOF, (B) PVB-P-MOF, and (C) PVP-P-MOF against the reciprocal of temperature (units of k_s is g mmol^{-1} min^{-1}).

values, summarised in Fig. 8. The coefficient of determination (R^2) for all the adsorption systems is very close to 1.0 (the lowest R^2 was 0.95 in Fig. 8A). This suggests that the extracted kinetic data reported in this work is capable of describing the adsorption systems accurately.

4.3.2. Temperature effect. While the rate constant (which is directly proportional to temperature) associated with CO_2 adsorption is an important parameter affecting the rate of adsorption, the driving force of adsorption ($q_e - q_t$) also has a significant impact on the overall rate. Since the equilibrium

Table 2 Equilibrium adsorption, rate constants, activation energies and pre-exponential factors associated with CO_2 adsorption on MOF (reported values are mean ± standard deviation)

		Temperature (°C)					
Material	Parameter[a]	25	40	60	80	E (kJ mol^{-1})	ln(A)[b]
NB-MOF	q_e	3.2 ± 0.1	3.0 ± 0.0	2.1 ± 0.1	1.4 ± 0.2	—	—
	k_f	1.6 ± 0.2	2.2 ± 0.3	2.5 ± 0.3	3.5 ± 0.3	11.3 ± 0.7	5.1 ± 0.2
	k_s	3.4 ± 1.1	3.5 ± 1.1	5.2 ± 1.2	8.4 ± 1.0	15.5 ± 4.0	7.3 ± 1.3
PVA-P-MOF	q_e	2.7 ± 0.0	2.3 ± 0.1	1.7 ± 0.0	1.1 ± 0.0	—	—
	k_f	2.7 ± 0.2	2.9 ± 0.2	3.6 ± 0.2	4.8 ± 0.3	9.5 ± 0.6	4.8 ± 0.2
	k_s	0.0	0.0	0.0	0.0	N/A	N/A
PVB-P-MOF	q_e	2.9 ± 0.1	2.7 ± 0.1	2.0 ± 0.1	1.4 ± 0.2	—	—
	k_f	1.6 ± 0.2	1.4 ± 0.1	2.0 ± 0.1	2.7 ± 0.2	9.2 ± 1.9	4.1 ± 0.7
	k_s	2.1 ± 0.1	2.8 ± 0.2	3.7 ± 0.2	7.1 ± 1.4	17.9 ± 3.4	7.9 ± 1.3
PVP-P-MOF	q_e	3.0 ± 0.1	2.6 ± 0.1	2.0 ± 0.1	1.3 ± 0.0	—	—
	k_f	2.2 ± 0.3	1.9 ± 0.30	2.7 ± 0.3	3.7 ± 0.4	9.6 ± 1.2	4.5 ± 0.5
	k_s	1.2 ± 0.4	1.7 ± 0.3	1.8 ± 0.5	3.0 ± 0.9	13.3 ± 2.3	5.5 ± 1.0

[a] Units of q_e, k_f and k_s are mmol g^{-1}, min^{-1} and g mmol^{-1} min^{-1}, respectively. [b] Units of A_f and A_s are min^{-1} and g mmol^{-1} min^{-1}, respectively.

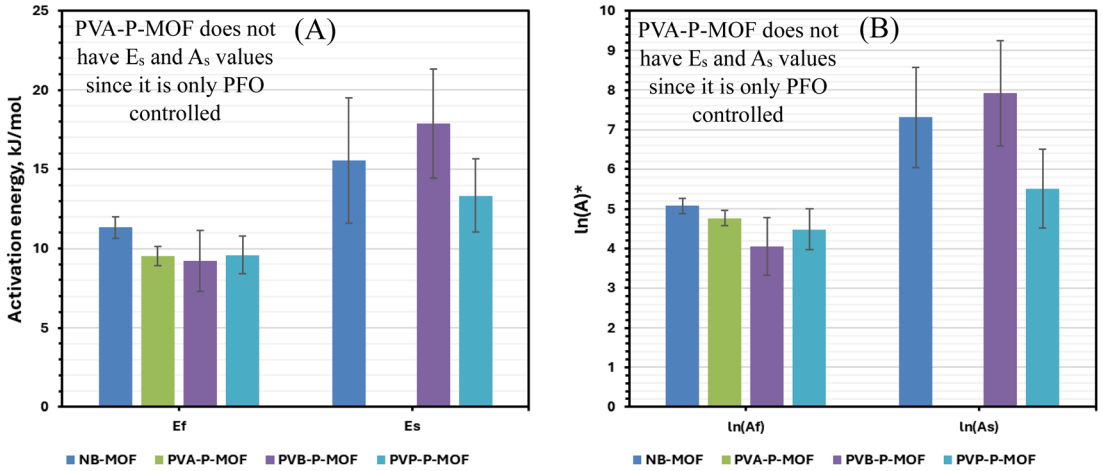

Fig. 6 (A) Activation energy and (B) pre-exponential factor associated with CO_2 adsorption (*units of A_f and A_s are min^{-1} and g $mmol^{-1}$ min^{-1}, respectively).

adsorption capacity q_e drops appreciably with temperature rise, the increase in temperature (causing an increase in the rate constant) does not necessarily mean that the rate of adsorption will increase. This is because the driving force of adsorption ($q_e - q_t$) is greatly reduced with temperature rise leading to an overall drop in the rate of adsorption. This effect is more pronounced at the higher temperatures, 60 and 80 °C. Fig. 9 summarises the temperature effect on the adsorption rate for all adsorption systems.

As expected, the adsorption rate drops with conversion for all temperatures due to the saturation of vacant sites in the MOF, resulting in a drop in the driving force ($q_e - q_t$) of adsorption. With the exception of PVB-P-MOF, the rate of adsorption at 60 and 80 °C is the lowest (slowest at 80 °C) followed by either 25 or 40° (depending on the material). No clear distinction can be seen between 25 and 40 °C; this is because in some cases, the drop in q_e with temperature increase is not large enough to cause the overall rate to drop, while simultaneously the rate constants (k_f and k_s) are increased at the higher temperature (40 °C). This can be seen in the case of NB-MOF, PVA-P-MOF, and PVB-P-MOF. For PVP-P-MOF, the drop in q_e (going from 25 to 40 °C) is large enough, such that even the increase in the rate constants is not enough to compensate for the drop in q_e, leading to a slightly faster rate of adsorption at 25 °C. However, as the temperature is increased further to 60 and 80 °C, a significant drop in the overall adsorption rate is observed (with 80 °C exhibiting the slowest rate of adsorption). This is because the drop in q_e at such temperatures is very large (see Fig. 3), which diminishes the driving force of adsorption ($q_e - q_t$). It is also important to highlight that the drop in the rate of adsorption follows a quadratic nature for all the materials except for PVA-P-MOF, which decays linearly. This is due to PVA-P-MOF being the only material which was completely governed by the linear PFO diffusion model, while the others showed mixed dependence on PFO and PSO (*i.e.*, MO model).

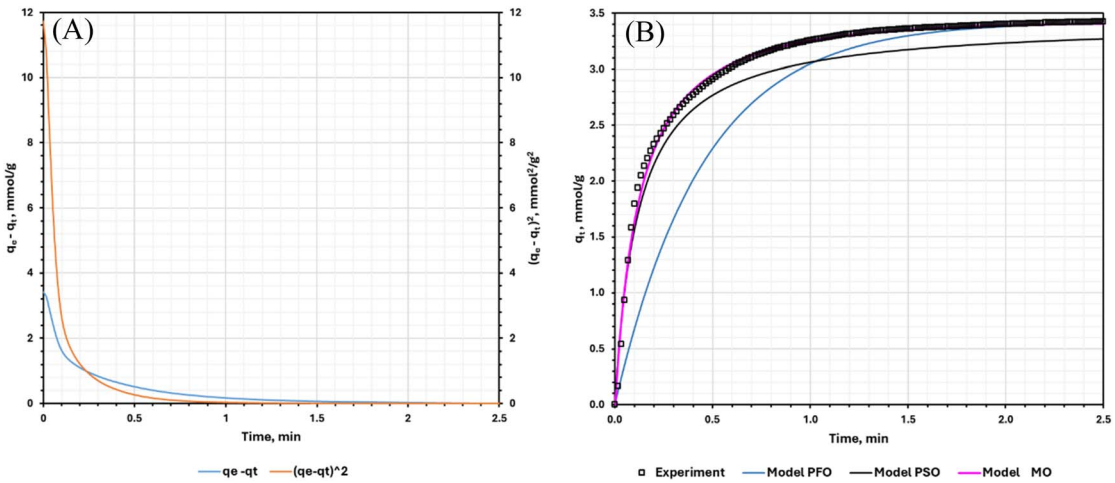

Fig. 7 (A) Weighing factors affecting the contribution of k_f and k_s on the overall adsorption rate and (B) data fitting using non-linear regression MO and linear regression PFO and PSO models (data in this figure is for NB-MOF).

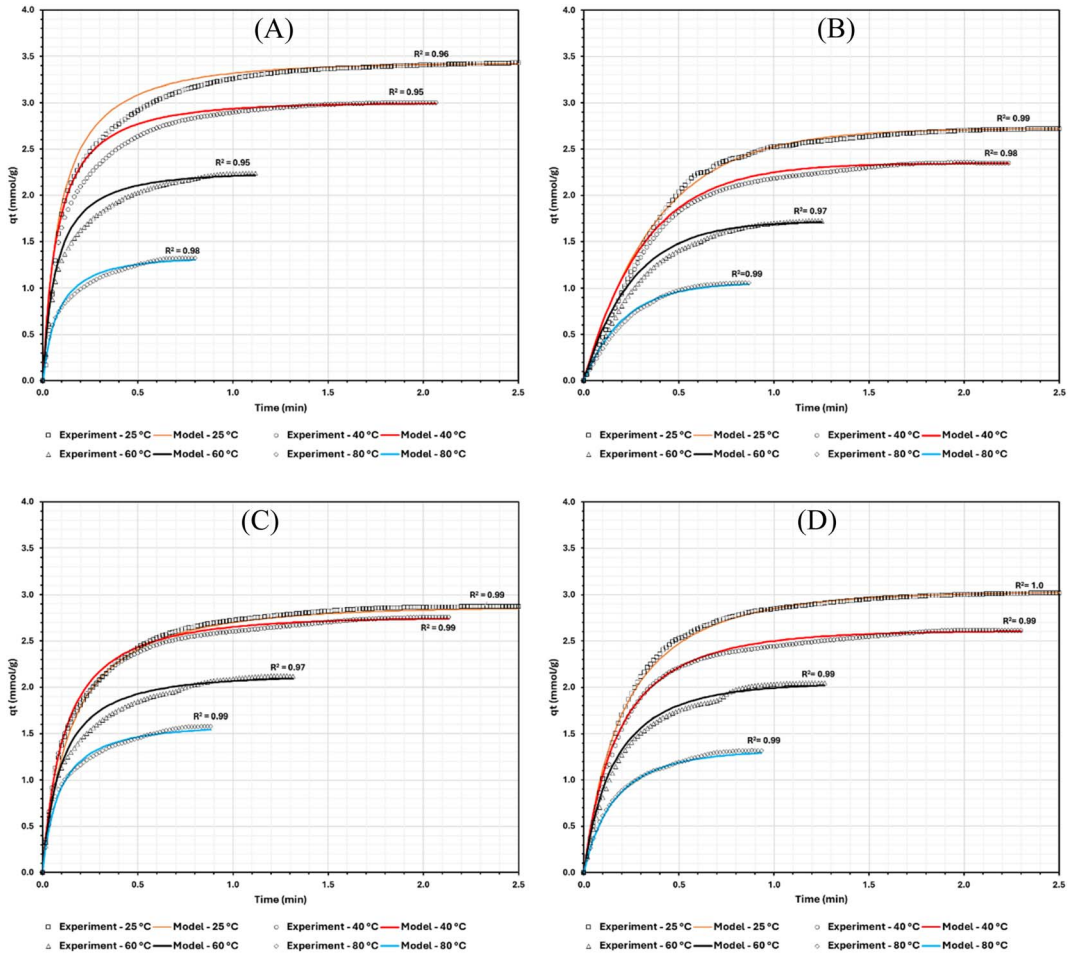

Fig. 8 Data fitting of (A) NB-MOF, (B) PVA-P-MOF, (C) PVB-P-MOF, and (D) PVP-P-MOF adsorption systems using extracted kinetic data appearing in Table 2 (q_t is mmol per g_MOF).

4.3.3. Geometry effect (powder *vs.* pellet). The effect of geometry on the rate of adsorption is presented in Fig. 10. With the exception of the 80 °C profile (Fig. 10D), NB-MOF exhibits the fastest adsorption rate followed by PVB-P-MOF, PVP-P-MOF, and PVA-P-MOF, respectively. This can be assigned to the significant drop in the surface area of the solid (lower gas–solid interaction surface) going from powder to pellet, thus causing the rate of adsorption to drop. Quantitatively, this behaviour can be related to the drop in the equilibrium adsorption capacity q_e going from NB-MOF to PVB-P-MOF, PVP-P-MOF, and PVA-P-MOF (see Fig. 3), with the latter exhibiting the lowest q_e value at all temperatures. The effect of changing the surface area (going from powder to pellet) can also be seen in Fig. 11, whereby the PSO rate constant (k_s) related to NB-MOF exhibits the highest value at all temperatures compared to all other materials (suggesting that the adsorption is majorly surface controlled).

In contrast, PVA-P-MOF exhibits a PSO rate constant of zero and a highest value of PFO rate constant (k_f) at all temperatures. This suggests that the adsorption on PVA-P-MOF is majorly diffusion controlled. These results agree with the rates of adsorption appearing in Fig. 10 such that the rate is hindered when the MOF is mixed with binders and shaped into pellets.

5. Example equipment design and application

5.1. Gas–solid molar balance

For a continuous operating process where CO_2 is being generated steadily, a possible design for CO_2 capture is a counter-current column, where fresh MOF is fed continuously from the top and CO_2 carrying gas is fed from the bottom as shown in Fig. 12.

At the bottom, CO_2 is being fed at a rate of N (mol min^{-1}), while at the top fresh MOF ($q_t = 0$) is being fed at a rate of m (kg min^{-1}). At steady state, q_t and n molar profiles are developed across the z-axis for a given column diameter (D), MOF flow rate (m), and kinetic parameters k_f, k_s, and q_e (depending on the controlling model). For an infinitesimally small section Δz (where $\Delta z \to 0$) along the length, a steady state mol balance on CO_2 can be performed:

$$n_z - n_{z+\Delta z} = mq_{tz+\Delta z} - mq_{tz} \quad (14)$$

Such that, n is the molar flow rate of CO_2 in mol min^{-1}, m is the mass flow rate of fresh MOF in kg min^{-1} and q_t is the adsorbed CO_2 on the MOF as defined in previous sections.

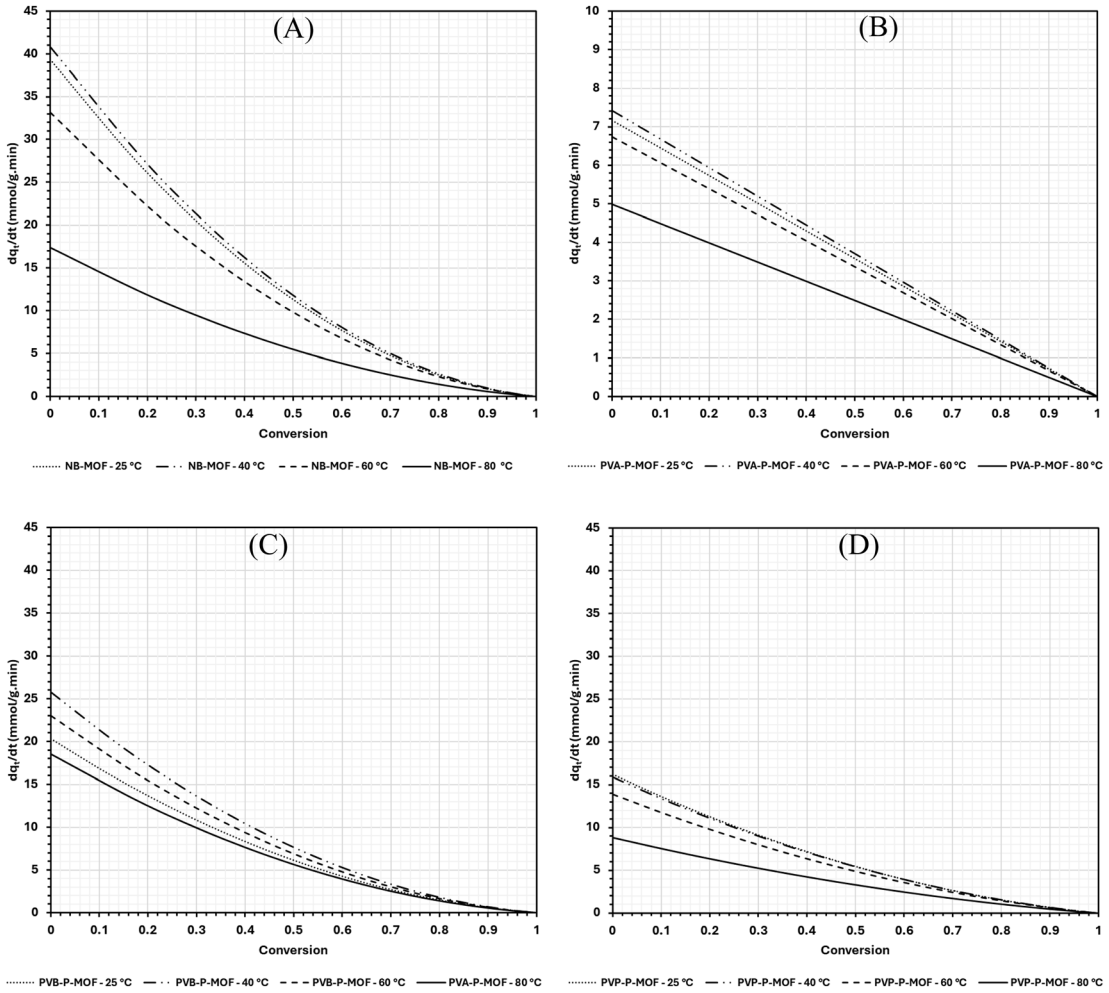

Fig. 9 Simulated adsorption rate against conversion generated using the kinetic data in Table 2, eqn (12) and (13) for the adsorption of CO_2 on (A) NB-MOF, (B) PVA-P-MOF, (C) PVB-P-MOF, and (D) PVP-P-MOF.

Dividing both sides with Δz and taking $\lim_{\Delta z \to 0} \frac{n_z - n_{z+\Delta z}}{\Delta z} = \frac{mq_{tz+\Delta z} - mq_{tz}}{\Delta z}$ yields:

$$\frac{dn}{dz} = -m\frac{dq_t}{dz} \tag{15}$$

Eqn (15) is the fundamental equation linking CO_2 gradient along the length of the column in the gas phase to the adsorbed CO_2 gradient in the solid phase.

5.2. Adsorbed CO_2 gradient $q_t(z)$

To be able to solve eqn (15) for the molar gradient of CO_2 in the gas phase $n(z)$, the gradient of the adsorbed CO_2 $q_t(z)$ needs to be developed first. $\frac{dq_t}{dz}$ appearing in eqn (15) can be linked to the previously developed adsorption rate $\frac{dq_t}{dt}$ as follows:

$$\frac{dq_t}{dt} = \frac{dz}{dt} \times \frac{dq_t}{dz} \tag{16}$$

Such that $\frac{dz}{dt}$ is the MOF velocity travelling down the column and can be denoted to by v, hence:

$$\frac{dq_t}{dz} = \frac{1}{v} \times \frac{dq_t}{dt} \tag{17}$$

$\frac{dq_t}{dt}$ appearing in eqn (17) is what we defined before in Section 2 and can be represented using the PFO, PSO, or MO models (depending on which model fits the adsorption data). For simplicity and for the sake of demonstration, the PFO model will be used in eqn (17) for the treatment here (the derivation for the other models for $q_t(z)$ is shown in the ESI†). The final results of $q_t(z)$ are all summarised in Table 3. Thus, eqn (17) can be written as follows:

$$\frac{dq_t}{dz} = \frac{1}{v} \times k_f(q_e - q_t) \tag{18}$$

Eqn (18) is a separable ODE which can be written as:

$$\int_0^{q_t} \frac{dq_t}{q_e - q_t} = \int_0^z \frac{k_f}{v} dz \tag{19}$$

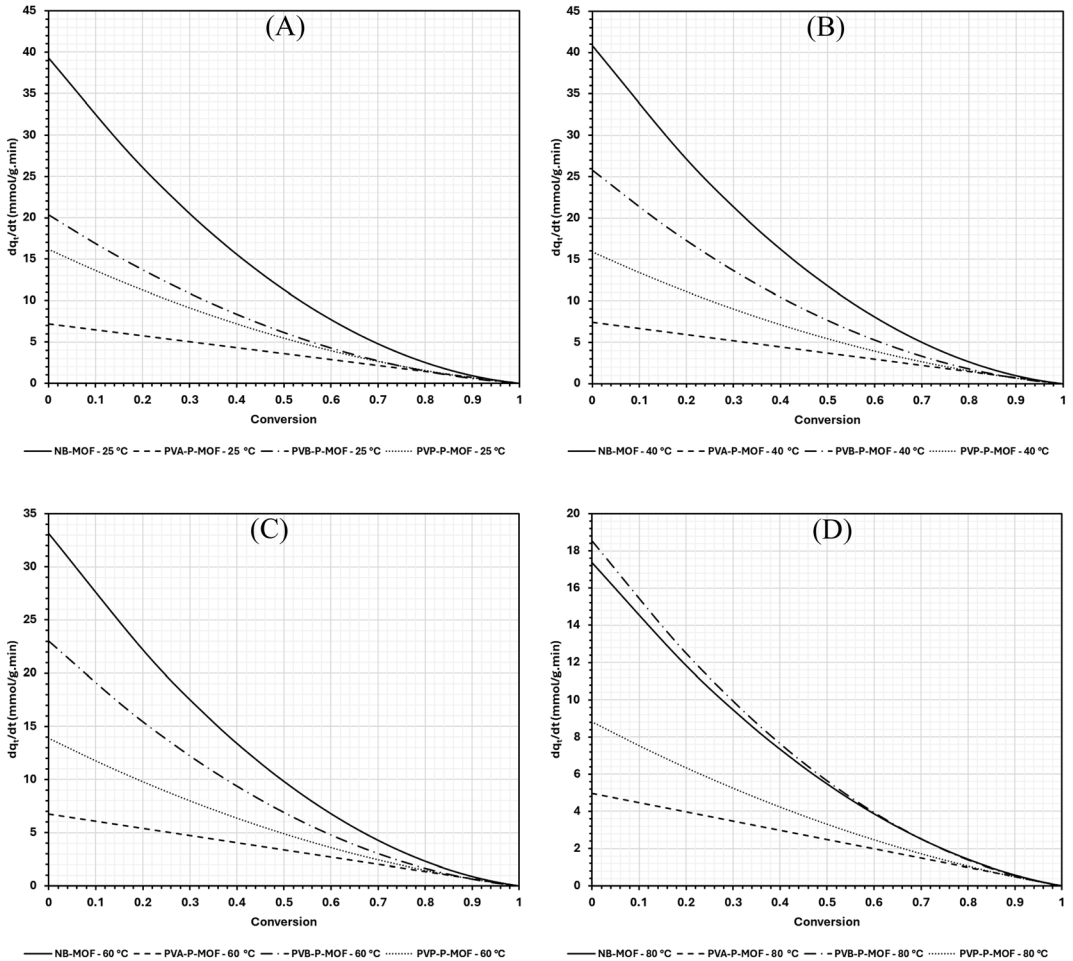

Fig. 10 Geometrical effect on the adsorption rate of CO_2 on powdered and pelletised MOF at temperatures (A) 25, (B) 40, (C) 60 and (D) 80 °C.

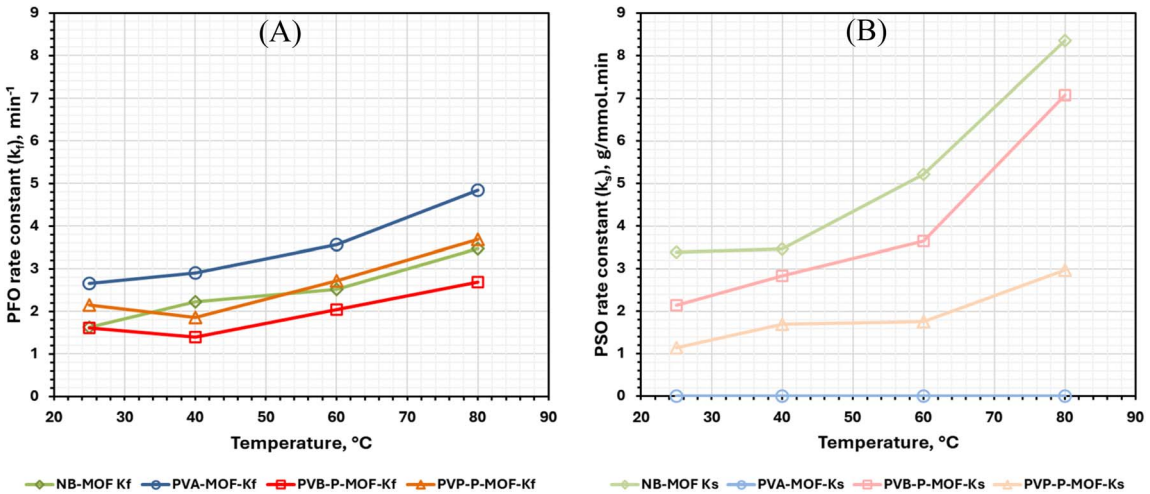

Fig. 11 (A) PFO (k_f) and (B) PSO (k_s) rate constants associated with the adsorption of CO_2 on NB-MOF, PVA-P-MOF, PVB-P-MOF, and PVP-P-MOF at different temperatures.

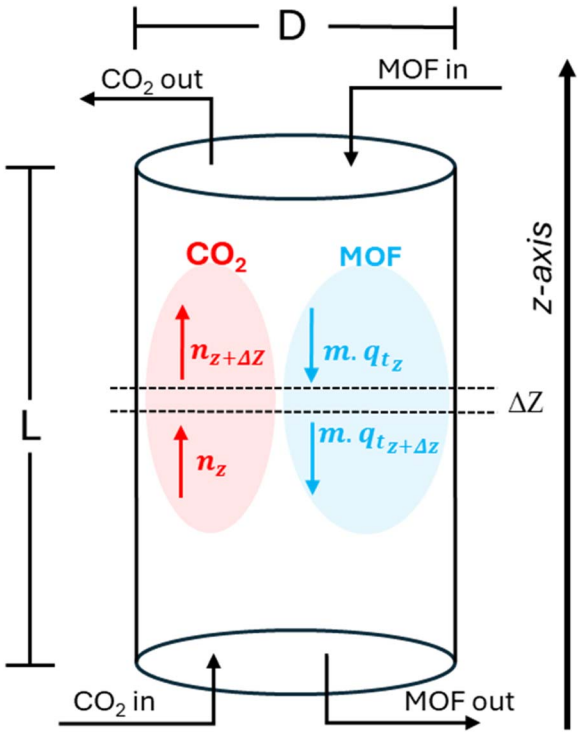

Fig. 12 Schematic of a continuous flow adsorption column where fresh MOF is fed at the top and process gas is fed from the bottom.

Table 3 The gradient of adsorbed CO_2 ($q_t(z)$) along the length of the adsorption column for different controlling mechanisms

Adsorption model	q_t gradient along the length of the column – $q_t(z)$
PFO	$q_t(z) = q_e\left(1 - e^{-\frac{k_f}{\nu}z}\right)$
PSO	$q_t(z) = q_e\left(1 - \frac{\nu}{\nu + q_e k_s z}\right)$
MO	$q_t(z) = q_e\left(1 - \frac{{k_f}^2}{({k_f}^2 + k_f k_s q_e)e^{\frac{k_f}{\nu}z} - k_f k_s q_e}\right)$

Solving the integral above and with the correct boundary conditions, the final equation yields:

$$\ln\left(\frac{q_e}{q_e - q_t}\right) = \frac{k_f}{\nu}z \tag{20}$$

which after re-arranging yields the final equation appearing in Table 3 (PFO).

It is important to highlight that the velocity (ν) of the MOF travelling down the column can be linked to its mass flow rate (m) as follows:

$$\nu = \frac{m}{\rho_b A} \tag{21}$$

Such that ρ_b is the bulk density of the MOF in the column and A is the cross-sectional area of the column.

5.3. Gaseous CO_2 gradient $n(z)$

Using the equations reported in Table 3, one can now solve for the gaseous CO_2 gradient along the column. When eqn (17) is substituted in eqn (15), it can now be written in terms of $\frac{dq_t}{dt}$ as follows:

$$\frac{dn}{dz} = -\frac{m}{\nu}\frac{dq_t}{dt} \tag{22}$$

Integrating both sides with the correct boundary conditions, yield:

$$\int_N^n dn = \int_0^z -\frac{m}{\nu}\frac{dq_t}{dt}dz \tag{23}$$

Eqn (23) is the general integral-form which can be used for any controlling model (PFO, PSO, or MO). The rate of adsorption $\frac{dq_t}{dt}$ can now be substituted from eqn (2) and (5) or (8) depending on the controlling mechanism. For demonstration, we will substitute the PFO model as follows:

$$\int_N^n dn = -\int_0^z \left(\frac{mk_f}{\nu}(q_e - q_t)\right)dz \tag{24}$$

$q_t(z)$ in Table 3 for the PFO model is now substituted in eqn (24) along with the value of ν (eqn (21)) giving:

$$\int_N^n dn = -\int_0^z \left(\rho_b A k_f \left(q_e - q_e\left(1 - e^{-\frac{k_f}{\nu}z}\right)\right)\right)dz \tag{25}$$

Such that ρ_b, A, k_f, and q_e are constants. After simplification, $n(z)$ can be written:

$$n(z) = N - \rho_b A q_e \nu\left(1 - e^{-\frac{k_f}{\nu}z}\right) \tag{26}$$

From eqn (26), it is shown that using the kinetic parameters q_e and k_f (in the case of PFO), one can predict the required MOF feeding speed ν, column area (*i.e.*, diameter), and column length to achieve a certain adsorption target (*i.e.*, to make the CO_2 molar flow rate drop from N to a fraction of it or to zero). It is extremely important, however, to note that the term residing next to N in eqn (26) $\left(\rho_b A q_e \nu\left(1 - e^{-\frac{k_f}{\nu}z}\right)\right)$ can in some cases yield values higher than N resulting in negative values of CO_2 molar flow rate which, in reality, is impossible. Thus, the length of the column (z) must be taken at the point at which the curve of $n(z)$ *vs.* z intersects with the x-axis (as shown in Fig. 13B and C). The reason for such a behaviour is because the equilibrium capacity q_e was reported in this study independently of CO_2

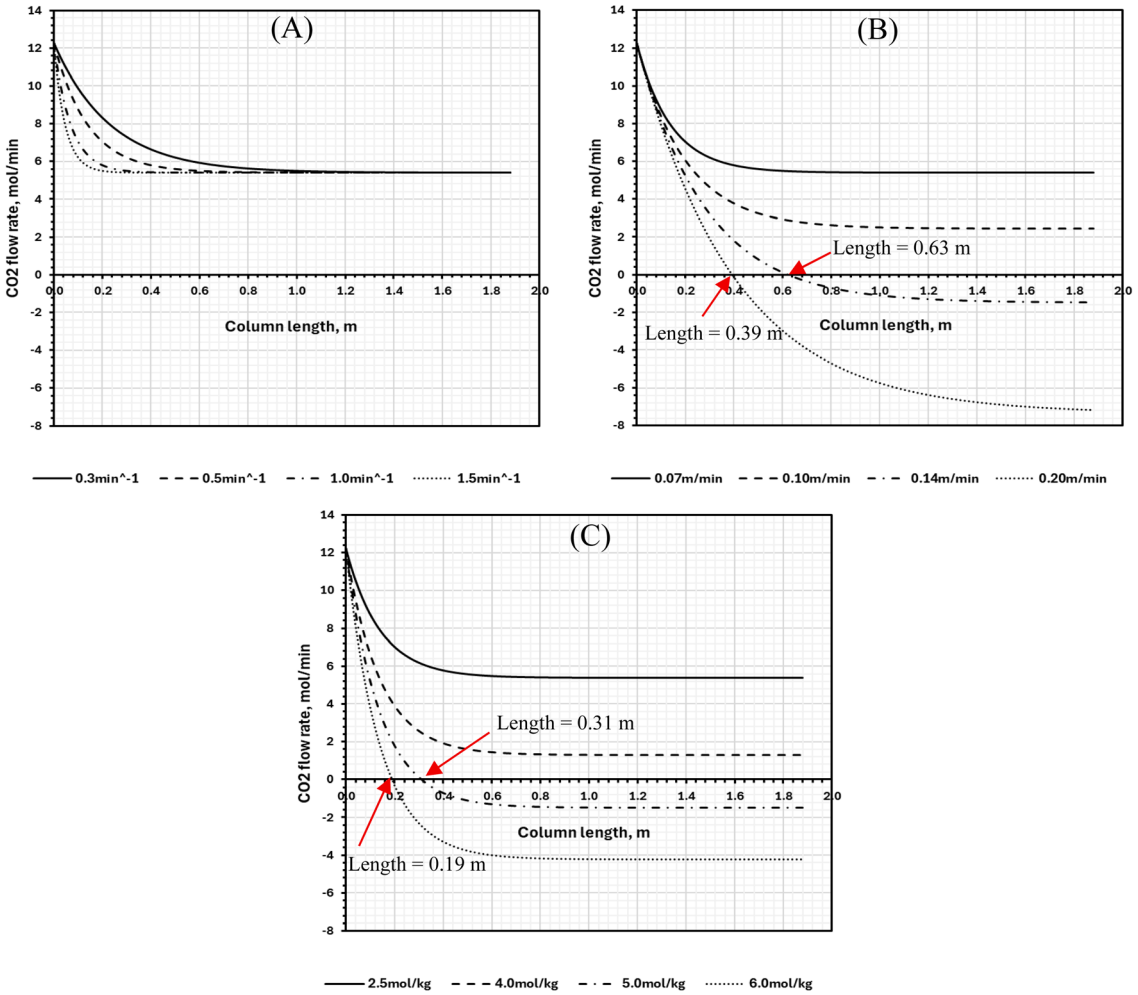

Fig. 13 CO_2 molar flow rate across the length of the column calculated at different (A) rate constant, (B) MOF feed velocity v and (C) MOF equilibrium capacity q_e (negative values should be neglected, and length should be taken from the intersection point with the x-axis as shown in (B and C)).

concentration in the gas phase; this behaviour, as mentioned before, was out of the scope of the current work and is to be investigated in future study.

The same treatment above can be conducted for a PSO or MO systems, however, in that case, $\frac{dq_t}{dt}$ in eqn (23) needs to be substituted for its corresponding model and the value of $q_t(z)$ afterwards should be substituted for the controlling model as shown in Table 3.

5.4. Case study

The exhaust line of a cement production plant typically contains 30 v/v% of CO_2 emitted from the burning of fossil fuel combined with the thermal decomposition of calcium carbonate in the calciner. If, for example, we are aiming to treat a branch of that line having a total volumetric flow rate of 1 m^3 min^{-1}, the CO_2 volumetric flow rate in that branch will be 300 L min^{-1}. If we assume that the gas temperature and pressure in that line were dropped to ambient values (1 atm and 298.15 K), an estimation of CO_2 molar flow rate can be done using the ideal gas equation of state:

$$N = \frac{PV}{RT} \quad (27)$$

Giving a value of $N = \frac{1 \times 300}{0.082 \times 298.15} = 12.3$ mol per min CO_2.

The molar flow of 12.3 mol min^{-1} will be assumed to be the initial flow rate (N) entering the adsorption column. For this simulation, the MOF bulk density and the column diameter were fixed at 800 kg m^{-3} and 0.25 m, respectively. A parametric sweep was done on different typical arbitrary values of the adsorption capacity q_e, MOF velocity v, and rate constant k_f as shown in Table 4.

Table 4 Parameters used to demonstrate the change in the molar flow rate gradient of CO_2 across the column length

Parameter	Typical values			
q_e (mol kg^{-1})	2.5	4.0	5.0	6.0
v (m min^{-1})	0.07	0.10	0.14	0.20
k_f (min^{-1})	0.5	0.3	1.0	1.5

For a certain MOF, if the kinetic analysis revealed that the process is controlled by a PFO model, then the design of the adsorption column will be governed by eqn (26). Results of the simulation using that equation for different parameters are presented in Fig. 13A–C. The values of the first column in Table 4 are fixed when any other parameter is varied. For example, when q_e is varied from 2.5 to 6.0 mol kg^{-1}, v and k_f are fixed at 0.07 m min^{-1} and 0.5 min^{-1}, respectively.

In Fig. 13A, increasing the rate constant k_f results in a drop in the column length needed to achieve a certain CO_2 molar flow rate value. For instance, to achieve a molar flow rate of 6 mol min^{-1} (molar flow drop of ~6.3 mol min^{-1}), a column length of 0.114, 0.171, 0.342, and 0.568 metres are needed for rate constants k_f 1.5, 1.0, 0.5 and 0.3 min^{-1}, respectively. Nonetheless, regardless of how much the rate constant value is increased, the final molar flow rate does not change with changing the rate constant and eventually plateaus at the same value (see Fig. 13A). In order for the final molar flow rate value to change, the MOF adsorption capacity q_e and/or MOF flow rate v have to change (this also applies to column diameter and MOF density which were fixed in this treatment). Contrary to the rate constant, increasing both q_e and v causes the final CO_2 molar flow rates to decrease. It is important to highlight that when negative CO_2 flow rates are encountered, they should be neglected, and the column length should be taken from the intersection point of the curve with the x-axis (see Fig. 13B and C). As mentioned earlier, this behaviour appears since q_e in this work was studied independently of CO_2 concentration in the gas phase (*i.e.*, the study was conducted in pure CO_2). This branch of kinetic effect is to be investigated in future studies. However, the data presented in this work unveils the effect of MOF geometry, binder and temperature effects. It also reports how these parameters can be utilised for adsorption column design which is relevant to industrial needs.

6. Conclusions

In this work, a comprehensive kinetic investigation carried out on the adsorption of CO_2 on UTSA-16(Zn) MOF with different solid geometries (powder/pellet), different binders and at different adsorption temperatures (25, 40, 60 and 80 °C). While it is well established that the processing and handling of solid materials is preferred in the pellet form due to several advantages such as lower bulk density, better flowability, and reduced pressure drop in packed beds, the following points need to be kept in mind which were concluded from this work:

- Generally, changing the geometry from powder to pellet resulted in a drop in the equilibrium adsorption capacity and the adsorption rate.
- It was confirmed that the adsorption processes are temperature locked (*i.e.*, they are related to activation energy barriers of E_f and E_s), whereby the rate constant increases with an increase in temperature. However, the overall adsorption rate can still decrease with an increase in temperature, due to a significant drop in q_e at the higher temperatures, leading to a drop in the adsorption driving force ($q_e - q_t$).
- Different behaviour was observed when different binders were used. For instance, PVA binder resulted in a drop in both the equilibrium adsorption capacity and the adsorption rate. This led to a change in the kinetic controlling mechanism from a MO model (where both surface adsorption and diffusion control the overall rate) to a PFO model, which is diffusion controlled only.
- The equilibrium adsorption capacity and the rate of adsorption are both affected by the type of the binder; PVB exhibited the highest capacity and adsorption rate followed by PVP and PVA.

The results presented here set a foundation for a better in depth understanding of CO_2 adsorption on MOFs and the impacts of pelletisation. Such data can also be used for equipment design (adsorption columns) to estimate optimum diameter, length, and MOFs residence time and/or flow rate to achieve certain adsorption limits as per the analyses reported in Section 5. Future research will extend the investigation to consider the kinetics of adsorption at different CO_2 concentrations in a carrier gas (*e.g.*, N_2) to account for the equilibrium dependency on CO_2 concentration.

Data availability

Data used in this article are available from the University of Nottingham repository, at **https://doi.org/10.17639/nott.7546**.

Author contributions

Sanad Altarawneh: conceptualization, investigation, methodology, validation, formal analysis, visualization, writing – original draft, writing – review & editing. John Luke Woodliffe: conceptualization, funding acquisition, investigation, methodology, validation, visualization, writing – original draft, writing – review & editing.

Conflicts of interest

There are no conflicts to declare.

Acknowledgements

The authors acknowledge and thank the Engineering and Physical Sciences Research Council (EPSRC, grant EP/W524402/1) for funding John Luke Woodliffe's Doctoral Prize Fellowship. The authors also thank the Nanoscale and Microscale Research Centre and the University of Nottingham (UoN) for providing funding and access to SEM (UoN and EPSRC grant EP/L022494/1) and TEM (UoN and EPSRC grant EP/W006413/1) expertise and instrumentation. In particular, the authors thank Michael Fay for TEM support.

References

1 IPCC, *Climate Change 2014: Impacts, Adaptation, and Vulnerability. Part A: Global and Sectoral Aspects. Contribution of Working Group II to the Fifth Assessment*

Report of the Intergovernmental Panel on Climate Change, Cambridge University Press, 2014.
2 G. C. C. S. Institute, *The Global Status of CCS: 2019*, 2019.
3 P. Markewitz, W. Kuckshinrichs, W. Leitner, J. Linssen, P. Zapp, R. Bongartz, A. Schreiber and T. E. Müller, *Energy Environ. Sci.*, 2012, **5**, 7281.
4 A. Samanta, A. Zhao, G. K. H. Shimizu, P. Sarkar and R. Gupta, *Ind. Eng. Chem. Res.*, 2012, **51**, 1438–1463.
5 O. M. Yaghi and H. Li, *J. Am. Chem. Soc.*, 1995, **117**, 10401–10402.
6 J.-R. Li, R. J. Kuppler and H.-C. Zhou, *Chem. Soc. Rev.*, 2009, **38**, 1477–1504.
7 L. J. Murray, M. Dincă and J. R. Long, *Chem. Soc. Rev.*, 2009, **38**, 1294.
8 P. Horcajada, R. Gref, T. Baati, P. K. Allan, G. Maurin, P. Couvreur, G. Férey, R. E. Morris and C. Serre, *Chem. Rev.*, 2012, **112**, 1232–1268.
9 H. Furukawa, K. E. Cordova, M. O'Keeffe and O. M. Yaghi, *Science*, 2013, **341**, 1230444.
10 R. Freund, O. Zaremba, G. Arnauts, R. Ameloot, G. Skorupskii, M. Dincă, A. Bavykina, J. Gascon, A. Ejsmont, J. Goscianska, M. Kalmutzki, U. Lächelt, E. Ploetz, C. S. Diercks and S. Wuttke, *Angew. Chem., Int. Ed.*, 2021, **60**, 23975–24001.
11 B. Dziejarski, J. Serafin, K. Andersson and R. Krzyżyńska, *Mater. Today Sustain.*, 2023, **24**, 100483.
12 S. B. Peh, S. Xi, A. Karmakar, J. Y. Yeo, Y. Wang and D. Zhao, *Inorg. Chem.*, 2020, **59**, 9350–9355.
13 S. Gaikwad, S.-J. Kim and S. Han, *J. Ind. Eng. Chem.*, 2020, **87**, 250–263.
14 J. L. Woodliffe, A.-L. Johnston, M. Fay, R. Ferrari, R. L. Gomes, E. Lester, I. Ahmed and A. Laybourn, *Mater. Adv.*, 2023, **4**, 5838–5849.
15 J. L. Woodliffe, J. Molinar-Díaz, R. Clowes, O. H. Hussein, E. Lester, R. Ferrari, I. Ahmed and A. Laybourn, *J. Environ. Chem. Eng.*, 2024, **12**, 114167.
16 V. B. López-Cervantes, M. L. Martínez, J. L. Obeso, C. García-Carvajal, N. S. Portillo-Vélez, A. Guzmán-Vargas, R. A. Peralta, E. González-Zamora, I. A. Ibarra, D. Solis-Ibarra, J. L. Woodliffe and Y. A. Amador-Sánchez, *Dalton Trans.*, 2025, **54**, 1646–1654.
17 M. Sadeghi, F. Esmaeilzadeh, D. Mowla and A. Zandifar, *Sep. Purif. Technol.*, 2024, **338**, 126534.
18 P. W. Dunne, E. Lester and R. I. Walton, *React. Chem. Eng.*, 2016, **1**, 352–360.
19 M. Rubio-Martinez, C. Avci-Camur, A. W. Thornton, I. Imaz, D. Maspoch and M. R. Hill, *Chem. Soc. Rev.*, 2017, **46**, 3453–3480.
20 A. Laybourn, A. M. López-Fernández, I. Thomas-Hillman, J. Katrib, W. Lewis, C. Dodds, A. P. Harvey and S. W. Kingman, *Chem. Eng. J.*, 2019, **356**, 170–177.
21 J. L. Woodliffe, R. S. Ferrari, I. Ahmed and A. Laybourn, *Coord. Chem. Rev.*, 2021, **428**, 213578.
22 S. M. Iveson, J. D. Litster, K. Hapgood and B. J. Ennis, *Powder Technol.*, 2001, **117**, 3–39.
23 B. Yeskendir, J.-P. Dacquin, Y. Lorgouilloux, C. Courtois, S. Royer and J. Dhainaut, *Mater. Adv.*, 2021, **2**, 7139–7186.
24 J. Zheng, X. Cui, Q. Yang, Q. Ren, Y. Yang and H. Xing, *Chem. Eng. J.*, 2018, **354**, 1075–1082.
25 V. Ntouros, I. Kousis, A. L. Pisello and M. N. Assimakopoulos, *Energies*, 2022, **15**, 1489–1510.
26 Z. Wang, L. Liu, Z. Li, N. Goyal, T. Du, J. He and G. K. Li, *Energy Fuels*, 2022, **36**, 2927–2944.
27 J. D. Martell, P. J. Milner, R. L. Siegelman and J. R. Long, *Chem. Sci.*, 2020, **11**, 6457–6471.
28 Y. Zhao, H. Ge, Y. Miao, J. Chen and W. Cai, *Catal. Today*, 2020, **356**, 604–612.
29 R. Hughes, G. Kotamreddy, A. Ostace, D. Bhattacharyya, R. L. Siegelman, S. T. Parker, S. A. Didas, J. R. Long, B. Omell and M. Matuszewski, *Energy Fuels*, 2021, **35**, 6040–6055.
30 Y. Ding, L. Ma, F. Zeng, X. Zhao, H. Wang, X. Zhu and Q. Liao, *Energy*, 2023, **263**, 125723.
31 M. Nedoma, H. Azzan, M. Yio, D. Danaci, I. Itskou, A. Kia, R. Pini and C. Petit, *Microporous Mesoporous Mater.*, 2024, **380**, 113303.
32 B. Singh, M. Kemell, M. J. Heikkilä and T. Repo, *Chem. Eng. J.*, 2025, **505**, 159416.
33 C. A. Grande, V. I. Águeda, A. Spjelkavik and R. Blom, *Chem. Eng. Sci.*, 2015, **124**, 154–158.
34 H. Thakkar, S. Eastman, Q. Al-Naddaf, A. A. Rownaghi and F. Rezaei, *ACS Appl. Mater. Interfaces*, 2017, **9**, 35908–35916.
35 M. M. Sadiq, M. Rubio-Martinez, F. Zadehahmadi, K. Suzuki and M. R. Hill, *Ind. Eng. Chem. Res.*, 2018, **57**, 6040–6047.
36 E. Hastürk, S.-P. Höfert, B. Topalli, C. Schlüsener and C. Janiak, *Microporous Mesoporous Mater.*, 2020, **295**, 109907.
37 H. Maher, T. H. Rupam, K. A. Rocky, R. Bassiouny and B. B. Saha, *Energy*, 2021, **238**, 121741.
38 R. Gaikwad, S. Gaikwad and S. Han, *J. Ind. Eng. Chem.*, 2022, **111**, 346–355.
39 S. Lagergren, *K. Sven. Vetenskapsakad. Handl.*, 1898, **24**, 1–39.
40 Y. Ho, D. A. J. Wase and C. C. F. Forster, *Water SA*, 1996, **22**, 219–224.
41 J. Wang and X. Guo, *J. Hazard. Mater.*, 2020, **390**, 122156.
42 K. V. Kumar and S. Sivanesan, *J. Hazard. Mater.*, 2006, **136**, 721–726.
43 M. I. El-Khaiary, G. F. Malash and Y.-S. Ho, *Desalination*, 2010, **257**, 93–101.
44 A. Marczewski, *Appl. Surf. Sci.*, 2010, **256**, 5145–5152.
45 X. Guo and J. Wang, *J. Mol. Liq.*, 2019, **288**, 111100.
46 S. Altarawneh, M. Al-Harahsheh, L. Ali, M. Altarawneh, O. H. Ahmed, A. Buttress, C. Dodds and S. Kingman, *Chem. Eng. J.*, 2024, 152873.
47 M. G. Plaza, C. Pevida, B. Arias, J. Fermoso, A. Arenillas, F. Rubiera and J. J. Pis, *J. Therm. Anal. Calorim.*, 2008, **92**, 601–606.
48 J. L. Woodliffe, J. Molinar-Díaz, B. Holland, O. H. Hussein, E. Lester and K. Robertson, *Chem. Eng. J.*, 2025, **503**, 158445.
49 C. F. Macrae, I. Sovago, S. J. Cottrell, P. T. A. Galek, P. McCabe, E. Pidcock, M. Platings, G. P. Shields,

J. S. Stevens, M. Towler and P. A. Wood, *J. Appl. Crystallogr.*, 2020, **53**, 226–235.
50 Q. Xie, F. Li, H. Guo, L. Wang, Y. Chen, G. Yue and D. L. Peng, *ACS Appl. Mater. Interfaces*, 2013, **5**, 5508–5517.
51 R. Gaikwad, S. Gaikwad and S. Han, *J. Ind. Eng. Chem.*, 2023, **126**, 444–453.
52 J. L. Woodliffe, M. Myszczynski, M. Fay, J. Molinar-Díaz, E. Lester and K. Robertson, *Chem. Eng. J.*, 2025, **510**, 161641.
53 O. Levenspiel, *Chemical Reaction Engineering*, John Wiley & Sons, 1998.